

# Discovery of Two Types of X-ray Dips in Cyg X-1

Y.X. Feng and Wei Cui

*Department of Physics, Purdue University, West Lafayette, IN 47907*

fengyx@physics.purdue.edu

cui@physics.purdue.edu

## ABSTRACT

We observed Cyg X-1 with *RXTE* contiguously over its 5.6-day binary orbit. The source was found to be in the hard state throughout the observation. Many intensity dips were detected in the X-ray light curves. We found that the dips fell into two distinct categories based on their spectral properties. One type exhibits strong energy-dependent attenuation of X-ray emission at low energies during a dip, which is characteristic of photoelectric absorption, but the other type shows nearly energy-independent attenuation. While the first type of dips are likely caused by density enhancement in an inhomogeneous wind of the companion star, as previous studies have indicated, the second type might be due to partial obscuration of an extended X-ray emitting region by optically thick “clumps” in the accretion flow. It is also possible that the latter are caused by a momentary decrease in the X-ray luminosity of the source, due, for instance, to a decrease in the mass accretion rate, or by Thomson scattering in highly ionized “clumps”. We discuss the implications of these scenarios.

*Subject headings:* binaries: general — stars: individual (Cygnus X-1) — X-rays: stars

## 1. Introduction

Cyg X-1 was the first astronomical system discovered to show strong evidence for a stellar mass black hole (Bolton 1972; Webster & Murdin 1972). It is a binary system with an orbital period of 5.6 days. The results from radial velocity measurements imply that the mass of the compact object exceeds the upper limit on the mass of a neutron star, so the compact object is inferred to be a black hole. A more recent study, based on spectrum synthesis, has derived a mass of about  $10 M_{\odot}$  for the black hole (Herrero et al. 1995). The

companion star has been identified as an O9.7 Iab supergiant (Walborn 1973; Gies & Bolton 1986), with a mass of about  $20 M_{\odot}$  (Herrero et al. 1995). Cyg X-1 is, therefore, intrinsically different from most known black hole candidates which contain only a low-mass companion star. This difference might be related to the fact that Cyg X-1 is a persistent X-ray source while those with a low-mass companion are exclusively transient sources.

The X-ray emission from Cyg X-1 is likely powered by accretion of material from the companion star by the black hole. In this case, the accretion flows are thought to follow a pattern that is intermediate between that of Roche-lobe overflow, as in low-mass systems, and that of wind accretion, which is common for high-mass systems (Gies & Bolton 1986). Such an accretion process is sometimes referred to as “focused wind accretion”, which can occur when the companion star is close to filling its Roche lobe (Friend & Castor 1982). The X-ray observations of Cyg X-1 have revealed that it has two distinct spectral states, hard and soft (see reviews by Oda 1977, Liang & Nolan 1984, Tanaka & Lewin 1995, Cui 1998, and Liang 1998). The source is usually found in the hard state, when its X-ray spectrum is relatively flat (with a typical power-law photon index of 1.5), but, occasionally, it makes a transition to the soft state, when the spectrum steepens significantly (to a typical photon index of 2.5).

In the hard state, the X-ray intensity of Cyg X-1 is strongly modulated by the binary motion (Wen et al. 1999; Brocksopp et al. 1999; Priedhorsky, Brandt, & Lund 1995; Holt et al. 1979), probably caused by varying amount of absorbing material along the line of sight through the stellar wind of the companion star. As expected, the intensity is found to reach a minimum at the times of superior conjunction of the black hole (when the companion star is in front of the black hole with respect to the line of sight), which is usually defined as orbital phase 0. It is, however, a very broad minimum, spanning about 26% of the orbit. In contrast, no X-ray orbital modulation is measurable in the soft state (Wen et al. 1999), which might be due to a significant change in the physical conditions of the wind (e.g., much higher ionization level) and/or in the geometry of the X-ray emitting region.

Besides the global orbital modulation of the X-ray emission, X-ray intensity dips are often seen in the light curves of Cyg X-1 (e.g., Pravdo et al. 1980; Remillard & Canizares 1984; Kitamoto et al. 1984; Bałucińska & Hasinger 1991; Ebisawa et al. 1996). The dips vary in duration from minutes to hours. The spectrum of the source hardens during a dip, implying that the dips probably originate in the photoelectric absorption of X-rays by the ambient medium. This is further supported by the detection of Fe K absorption edge in the dip spectrum in some cases (Kitamoto et al. 1984). The absorbing column density can increase by more than one order of magnitude during a dip (Kitamoto et al. 1984; Bałucińska-Church et al. 1997). The distribution of dips against orbital phases shows a

prominent peak around phase 0 (Bałucińska-Church et al. 2000), implying an origin of the dips in the stellar wind from the companion star.

In this paper, we present results from a long observation of Cyg X-1 with the *Rossi X-Ray Timing Explorer* (RXTE) over one complete 5.6-day orbital cycle. Many intensity dips were detected. The large collecting area of the Proportional Counter Array (PCA) aboard *RXTE* made it possible to conduct a more detailed investigation of spectral evolution of the source during some of the strong dips, as well as to carry out orbital-phase-resolved spectroscopy to quantify the variation in the column density over an orbital cycle.

## 2. Data

For six consecutive days (2000 January 5–11) Cyg X-1 was observed with the large-area detectors aboard RXTE, with usual interruptions because of earth occultation and passage of the satellite through the South Atlantic Anomaly. The data were collected for an effective exposure time of about 240 ks. Judging from the long-term ASM/RXTE light curves of the source (both the flux and hardness ratios), Cyg X-1 was in its usual hard state when our pointed RXTE observations were made.

Besides the PCA, *RXTE* also carries another pointing instrument, the High-Energy X-ray Timing Experiment, which covers a nominal energy range of 15–250 keV. For this investigation, only the PCA data (2–60 keV) were used, because we are primarily interested in spectral changes at low energies. The PCA consists of five *Proportional Counter Units* (PCUs). Not all PCUs were turned on throughout the observation, because of technical difficulties with some of the PCUs. Consequently, the number of PCUs used varied between 3 and 5. Because of this, it was necessary to break up the observation into a number of segments and to analyze data for each segment separately.

## 3. Analyses and Results

Both spectral and timing analyses were carried out using the *Standard 2* data (which has a timing resolution of 16 seconds). We used *ftools v5.0*, as well as the calibration files and background models that accompanied this release of the software, to extract X-ray spectra and light curves of Cyg X-1. The quality of the background models was examined by comparing an overall spectrum (source plus background) with the corresponding model background spectrum. The two should overlap each other at the highest energy channels, since the counts in those channels should be entirely due to the background. We found that

background modeling was satisfactory, except for a couple of cases where renormalization of the background was necessary.

### 3.1. X-ray Dips

We made a light curve for each of the following energy bands: 3–6 keV, 6–15 keV, and 15–60 keV, using data from all PCUs (and all xenon layers) that were turned on for a segment of the observation. A corresponding background light curve was then constructed from the models and was subtracted from the overall light curve to obtain the light curve of the source for a particular energy band. The light curve of each segment was then normalized to count rates per PCU, and all segments were pieced together to obtain the final light curve for the entire observation. We also computed hardness ratios by taking the ratio of the light curves in two energy bands (higher energy band over lower energy band). The hardness ratios are useful in providing crude information about the spectral properties of a source.

The light curves of Cyg X-1 reveal frequent occurrences of a brief decrease in the intensity of the source. These are X-ray dips. In most cases, the hardness ratios indicate that the spectrum of Cyg X-1 hardens during a dip, implying that the dips are caused by additional absorption. As an example, Figure. 1 shows a segment of the light curves where two dips are clearly visible (on top of an X-ray flare). As a matter of fact, the dips manifest themselves much more prominently as peaks in the hardness ratio plots, which are also shown in the figure. Note that we have plotted orbital phases instead of times to emphasize the distribution of dips over the orbital cycle. For this purpose, we have used the most updated ephemeris of Cyg X-1 (Brocksopp et al. 1999). The range of orbital phases covered by our observations is between 0.50 and 1.60.

To obtain a complete sample of dips, we used the 3–6 keV light curve alone, because it is most sensitive to absorption dips and the data is of the highest quality (compared to light curves in higher energy bands). We adopted the following algorithm to detect dips. First, we smooth the light curve by a running boxcar with a width of 3 time bins (or 48 s), to minimize intrinsic variability of the source. Second, we scan over the entire light curve for all “local minima”. A local minimum is defined as a point with two higher adjacent neighbors. Third, we compare each local minimum with its next closest neighbor on each side. This process continues until two points on each side are found to be more than  $20\sigma$  higher than the local minimum itself (where  $\sigma$  is the error bar of the local minimum). A dip is then identified. On the other hand, the process stops, if one neighbor on either side is lower than the local minimum or if the time interval examined exceeds 300 time bins (or 4.8 ks) or reaches the overall length of a data segment, before the  $20\sigma$  threshold is reached. We then move onto

the next local minimum, until all minima in the list have been examined. The choice of a relatively high detection threshold is to minimize confusion due to the intrinsic variability of the source. Since the main objective of this investigation is to study the spectral properties of dips in a more detailed manner than what has been done previously (rather than focusing on the frequency of the dips; see (Bałucińska-Church et al. 2000)), the reliability of detection is much more important than the number of dips that we can detect. We note that our algorithm is clearly biased against dips of very short durations (less than 80 s) or those of very long durations (greater than 4.8 ks or the duration of a data segment). However, it is very difficult to improve the situation, because the detection of short-duration dips is limited by the intrinsic variability of the source and the detection of long-duration ones is complicated by coverage gaps in the data.

We detected a total of 33 dips. To examine their distribution over the binary orbit, we divided the orbit into 20 phase bins and computed the *normalized* number of dips in each phase bin (which is the number of dips detected divided by the fractional coverage of the phase bin). The normalization is necessary because there are gaps in the light curve and thus the coverage is incomplete for all phase bins (note that each phase bin corresponds to about 0.28 days or 6.7 hours). The results are shown in Figure 2. The overall shape of the distribution, such as the apparent asymmetry about phase 0, is in general agreement with that derived previously (Bałucińska-Church et al. 2000), although the statistics are very limited here. The asymmetry in the distribution might be a manifestation of enhanced “clump” formation in the leading hemisphere of the stellar wind, because of the compression of the wind by orbital motion.

The duration of the dips varies greatly. Figure 3 shows a dip that has the longest duration among all detected. It should be noted that this dip was *not* detected by the algorithm, because of its long duration as well as the data gaps present. It is interesting that it occurred almost exactly at phase 0. Unfortunately, the presence of gaps in the data makes it impossible to derive its duration accurately. The profile of a dip can be quite complex, certainly not necessarily symmetric. Figure 4 shows an example of such a dip. Sub-structures within the dip are quite apparent (although it can also be argued that it is a superposition of two smaller dips).

Upon a closer examination of the dips detected, we found that they fell into two distinct categories, based on their spectral properties. While the majority of the dips show strong spectral variation over the duration of dipping activity (see the hardness ratio plots in Figures 1, 3, and 4), there are some dips that show little spectral variation. We refer to the former as type A and the latter as type B. As examples, Figures 5 and 6 show the light curve and hardness ratios of two type B dips of quite different durations. It is clear that type B dips

can be comparable in depth to type A ones (e.g., comparing Figure 1 and Figure 6) but they show much less spectral variation (if any at all). Of the 33 dips detected, 4 dips are quite convincingly type B. They seem to distribute randomly over the orbit: one is around phase 0.637, one around phase 0.830, one around phase 0.995, and one around 1.148, but we do not have sufficient statistics to address this issue with confidence.

### 3.2. Dip Spectra

We proceeded to carry out more detailed spectral analyses and modeling for some of the strong dips. We divided the overall light curve into dip and non-dip time intervals (with gaps between the two to ensure the quality of the dip spectra). We then extracted a source spectrum for each time interval by combining data from all PCUs (and all xenon layers) that were on during the observation. To strengthen some of the conclusions drawn from the hardness ratios in a model-independent manner, we simply divided the spectrum of the source during a dip by the average non-dip spectrum. For illustration, Figure 7 shows the results for a type A dip and a type B dip, respectively.

We can see that the spectrum of the type A dip rolls over much faster than the non-dip spectrum below about 6 keV, indicating the need for additional absorbing material intrinsic to the binary system. It is interesting to notice that the dip spectrum never fully recovers to the non-dip spectrum even at high energies. This seems to signify the importance of Thompson scattering in attenuating X-ray flux (at a few percent level). The presence of sufficient number of electrons to participate in the scattering process would imply that the absorbing medium is perhaps highly ionized, which has been suggested previously (Pravdo et al. 1980; however, see Kitamoto et al. 1984; Bałucińska-Church et al. 1997).

To be more quantitative, we fit the spectra with an empirical model that was used in previous studies of Cyg X-1 (Ebisawa et al. 1996; Cui et al. 1997). First, we fit the non-dip spectrum with a broken power law (plus a Gaussian function, which is needed to minimize residuals between 6–7 keV). A detailed discussion of physical models is beyond the scope of this paper. Here we only focus our attention on how the column density varies in a dip. The model describes the spectrum quite well. The inferred column density is  $0.8 \pm 0.4 \times 10^{22} \text{ cm}^{-2}$ , which is in general agreement with previous measurements (e.g., Bałucińska & Hasinger 1991; Ebisawa et al. 1986; Cui et al. 1998). We then applied the best-fit model for the non-dip spectrum to the dip spectrum by fixing all model parameters except for the column density. This procedure is necessary because the quality of the dip spectrum is not adequate for constraining so many parameters in the model, but there is no physical justification for doing so. This only represents an attempt to quantify the amount

material in the binary system that caused an absorption dip. The model fits the dip spectrum quite well. The inferred column density for the dip is  $1.7 \pm 0.1 \times 10^{22} \text{ cm}^{-2}$ , which roughly doubles the interstellar value. We note that this is only the average column density for the dip; the peak value can be much higher.

The situation for type B dips is quite different. For the type B dip shown in Figure 5, the ratio of the dip and non-dip spectra is nearly flat up to at least 20 keV, above which the statistics become quite poor. If we average all data points above 20 keV, the average level seems to lie above that for data points below 20 keV. The lack of a strong energy dependence of the ratio at low energies indicates that the observed attenuation cannot be due to photoelectric absorption. There are at least three possible scenarios that might explain the type B dips. The first scenario attributes the type B dips to partial covering of an extended X-ray emitting region by material that is totally opaque. The second one is that the source experiences a momentary decrease in its luminosity during a type B dip, due, for instance, to a sudden decrease in the mass accretion rate. The third possibility is that the type B dips originate in pure Thompson scattering, implying that the clumps must be almost fully ionized.

### 3.3. Orbital Variation in Column Density

To investigate the global orbital modulation of X-ray emission previously seen (e.g., Wen et al. 1999), we binned the observation into 10 orbital phases. For each orbital phase, we extracted a spectrum of the source, as before, but used data only from the first xenon layer of each PCU to minimize calibration uncertainties, since it is the most accurately calibrated among all xenon layers. The trade-off is that we lost spectral coverage at energies above about 25 keV. We can afford such a loss here, because we are only interested in spectral variation at the lowest energies due to photoelectric absorption.

For each orbital phase, we fit the spectrum with the same model described in the previous section (broken power law plus Gaussian function) and the results are satisfactory. Figure 8 shows the inferred column density at different orbital phases. Although the column density seems to be higher near superior conjunction, large uncertainties prevent us from drawing a definitive conclusion, especially in the presence of other high points, e.g., at phase 1.3, which may or may not be real. The large uncertainty in determining the column density arises mostly from the fact that the sensitivity of the PCA drops precipitously below about 3 keV. Bałucińska-Church et al. (2000) computed variation in column density through the stellar wind due to orbital motion, based on a simple wind geometry, for two extreme cases with and without the suppression of radiatively-driven wind. Our results seem to lie between

those two cases (comparing Figure 8 with Figure 7 of Bałucińska-Church et al. 2000).

#### 4. Discussion

As mentioned in the introduction, the phenomenon of X-ray intensity dips in Cyg X-1 is well known and well studied. Over the years, a rich database has been built up for this famous black hole candidate. The database is essential for a systematic study of dips, whose occurrence is somewhat unpredictable and is thus easy to miss in a brief pointed observation. The distribution of the dips over a binary orbital cycle has been reliably established recently (Bałucińska-Church et al. 2000): most of the dips occur near superior conjunction of the X-ray source, but dipping activity has also been seen at orbital phases far from superior conjunction. Our results are consistent with that. We went a step further in this study. We carried out a long observation of Cyg X-1 over one entire orbital period with the large-area detectors aboard *RXTE*. The data allowed us to conduct more detailed spectral analyses of the dipping phenomenon as well as phase-resolved spectroscopy to quantify the variation in the column density over an orbit.

The main result of this investigation is the recognition of the existence of two types of dips. The spectrum of type A dips shows an energy-dependent reduction at low energies that is characteristic of photoelectric absorption. Detailed spectral modeling shows that the only difference between the spectrum of type A dips and the average non-dip spectrum seems to be the presence of additional column density during a dip. We stress, however, that our data is not of sufficient quality to warrant more complicated modeling, as has been done previously (e.g., Ebisawa et al. 1996). The type A dips seem to occur preferentially around the times of superior conjunction of the black hole. The spectrum of type B dips, on the other hand, shows almost an energy-independent reduction at low energies. Therefore, these dips cannot possibly be due to photoelectric absorption. Moreover, the type B dips appear to distribute randomly over the binary orbit.

Type A dips are much more common than type B dips. They are probably produced by density enhancement in an inhomogeneous wind from the companion star, since the column density changes only moderately during such a dip. They occur more frequently around superior conjunction probably because the line-of-sight follows a longer path through the denser part of the wind (however, see Blondin & Woo 1995). The inhomogeneities in the wind can be caused by a variety of physical processes (see Bałucińska-Church et al. 2000 for a few examples). It remains to be seen whether the observed global orbital modulation of X-ray emission is entirely due to the presence of such dips.

Type B dips might be caused by partial covering of an extended X-ray emission region by an opaque “screen”. In the context of Comptonization models (e.g., review by Liang 1998 and references therein), the presence of an extended emitting region may not be unreasonable for Cyg X-1. The question is what could physically serve as an opaque “screen” to produce the observed type B dips. The answer may lie in the fact that Cyg X-1 is a high-mass X-ray binary (HMXB), in which the mass accretion process is probably mediated by stellar wind from the massive companion star. Numerical simulations of mass accretion in HMXBs show that a tidal stream develops when the companion star is close to filling its Roche lobe and that the stream trails behind the compact object due to the Coriolis force (Blondin et al. 1991). The density in the stream is shown to be as high as 20–30 times the ambient wind density. Since the obscuration of X-rays occurs close to the accretion disk in this case, it is not expected to be very sensitive to the binary motion. Now, the question is whether this scenario can be applied to Cyg X-1, whose orbit is only moderately inclined, with a probable inclination angle of  $30^\circ$ – $40^\circ$  (Bolton 1975; Guinan et al. 1979; Daniel 1981). A full three-dimensional simulation would be required to show the scale height of the tidal streams. We note that the inclination angle remains to be poorly determined for Cyg X-1, which is one of the largest contributors to the uncertainty in determining the mass of the compact object. For instance, the optical polarization measurements imply a wide range of  $25^\circ$ – $70^\circ$  (e.g., Long et al. 1980).

Type B dips might also be due to a sudden decrease in the mass accretion rate, causing a decrease in the X-ray luminosity of the source itself. This could, in principle, occur, since, after all, the intrinsic variability of the source is generally thought to be due to fluctuation in the mass accretion rate. However, for Cyg X-1 (and black hole candidates in general), a change in X-ray flux is generally accompanied by a change in spectral hardness. In fact, it has been shown that in the hard state the flux and spectral hardness are, to some degree, anti-correlated (e.g., Wen et al. 2001). However, the correlation is quite weak, so our results cannot rule out this possibility.

It is also possible that type B dips are produced by (nearly) pure Thomson scattering of X-rays in highly ionized dense clumps in the wind. Given that the cross section for photoelectric absorption is, on average, more than two orders of magnitude larger than the Thomson cross section, the density of a clump that produces a type B dip is required to be more than two orders of magnitude larger than that of a clump that produces a type A dip of comparable depth (assuming that the clumps are comparable in size). To obtain an ionization parameter that is, for instance, a factor of 100 larger for type B clumps than for type A clumps, we would then require that the former are, on average, more than 100 times closer to the X-ray source. If so, this scenario could also explain why the type B dips are much less dependent of orbital phases.

Finally, we made an attempt to quantify how the column density varies with orbital motion by carrying out orbital-phase-resolved spectroscopy. The results seem to indicate that the column density is higher at superior conjunction, although error bars are too large for us to be definitive about it. The issue can be resolved by a similar observation with detectors of much improved low-energy response and spectral resolution, such as those aboard *Chandra* and *XMM*. Much improved spectral resolution of these detectors will also allow the detection of absorption edges, which provides means of determining column density in a manner that is independent of continuum modeling (Schulz et al. 2001). Furthermore, the highly eccentric orbits of these satellites allow long un-interrupted observations, which is very much important for studying the distribution of dips over a binary orbit.

We wish to thank Dr. Douglas Gies, the referee, for many helpful comments. In particular, he suggested that type B dips might be caused by a change in the luminosity of the source and that the asymmetry in the dip distribution might be due to the compression of the stellar wind by orbital motion. This work was supported in part by NASA through grants NAG5-9098 and NAG5-9998.

## REFERENCES

- Bałucińska, M. & Hasinger, G. 1991, *A&A*, 241, 439
- Bałucińska-Church, M., Takahashi, T., Ueda, Y., Church, M. J., Dotani, T., Mitsuda, K., & Inoue, H. 1997, *ApJ*, 480, L115
- Bałucińska-Church, M., Church, M. J., Charles, P. A., Nagase, F., LaSala, J., & Barnard, R. 2000, *MNRAS*, 311, 861
- Blondin, J. M., Stevens, I. R., & Kallman, T. R. 1991, *ApJ*, 371, 684
- Blondin, J. M., & Woo, J. 1995, *ApJ*, 445, 889
- Bolton, C. T. 1972, *Nature*, 235, 271
- Bolton, C. T. 1975, *ApJ*, 200, 269
- Brocksopp, C., Tarasov, A. E., Lyuty, V. M., & Roche, P. 1999, *A&A*, 343, 861
- Cui, W., Heindl, W. A., Rothschild, R. E., Zhang, S. N., Jahoda, K., & Focke, W. 1997, *ApJ*, 474, L57
- Cui, W. 1998, in *ASP. Conf. Ser. 161, High-Energy Processes in Accreting Black Holes*, ed. J. Poutanen & R. Svensson, (San Francisco: ASP), 97 (astro-ph/9809408)
- Cui, W., Ebizawa K., Dotani T., and Kubota A., 1998, *ApJ*, 493, L75

- Daniel, J. Y. 1981, *A&A*, 94, 121
- Ebisawa, K., Ueda, Y., Inoue, H., Tanaka, Y., & White, N. E. 1996, *ApJ*, 467, 419
- Friend, D. B., & Castor, J. I. 1982, *ApJ*, 261, 293
- Gies, D. R. & Bolton, C. D. 1986, *ApJ*, 304, 371
- Guinan, E. F., Dorren, J. D., Siah, M. J., & Koch, R. H. 1979, *ApJ*, 229, 296
- Herrero, A., Kudritzki, R.P., Gabler, R., Vilchez, J. M., & Gabler, A. 1995, *A&A*, 297, 556
- Holt, S. S., Kaluzienski, L. J., Boldt, E. A., & Serlemitsos, P. J. 1979, *ApJ*, 233, 344
- Kitamoto, S., Miyamoto, S., Tanaka, Y., Ohashi, T., Kondo, Y., Tawara, Y., & Nakagawa, M. 1984, *PASJ*, 36, 731
- Liang, E. P. & Nolan, P. L., 1984, *Space Sci. Rev*, 38, 353
- Liang, E. P. 1998, *Physics Reports*, 302, 67
- Long, K. S., Chanan, G. A., & Novick, R. 1980, *ApJ*, 238, 710
- Oda, M. 1977, *Space Sci. Rev.*, 20, 757
- Pravdo, S. H., White, N. E., Becker, R. H., Kondo, Y., Boldt, E. A., Holt, S. S., Serlemitsos, P. J., & McCluskey, G. E. 1980, *ApJ*, 237, L71
- Priedhorsky, W. C., Brandt, S., Lund, N. 1995, *A&A*, 300, 415
- Remillard, R. A. & Canizares, C. R. 1984, *ApJ*, 278, 761
- Schulz, N. S., Cui, W., Canizares, C. R., Marshall, H. L., Lee, J. C., Miller, J. M., & Lewin, W. H. G. 2001, *ApJ*, submitted
- Tanaka, Y., & Lewin, W. H. G. 1995, in *X-ray Binaries*, ed. W. H. G. Lewin, J. van Paradijs, & E. P. J. van den Heuvel (Cambridge U. Press, Cambridge), 126
- Walborn, N.R., 1973, *AJ*, 78, 10, 1067
- Webster, B. L., & Murdin, P. 1972, *Nature*, 235, 37
- Wen, L., Cui, W., Levine, A. M., & Bradt, H. V. 1999, *ApJ*, 525, 968
- Wen, L., Cui, W., & Bradt, H. V. 2001, *ApJ*, 546, 105

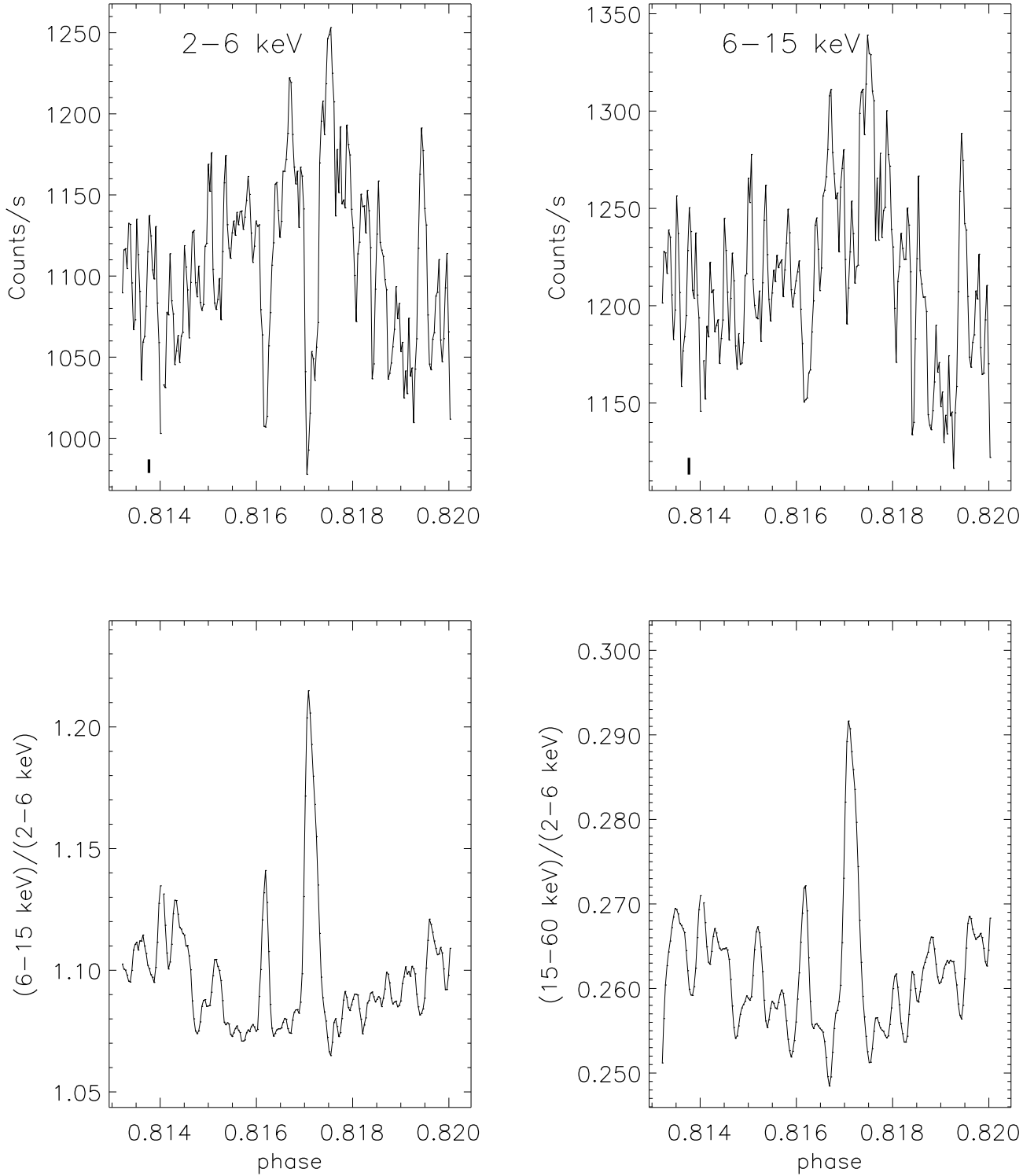


Fig. 1.— X-ray dips in Cyg X-1. The time bin of each data point is 16 s. The light curves have been smoothed by a running boxcar of a width of 3 time bins. The typical size of error bars is shown for each light curve.

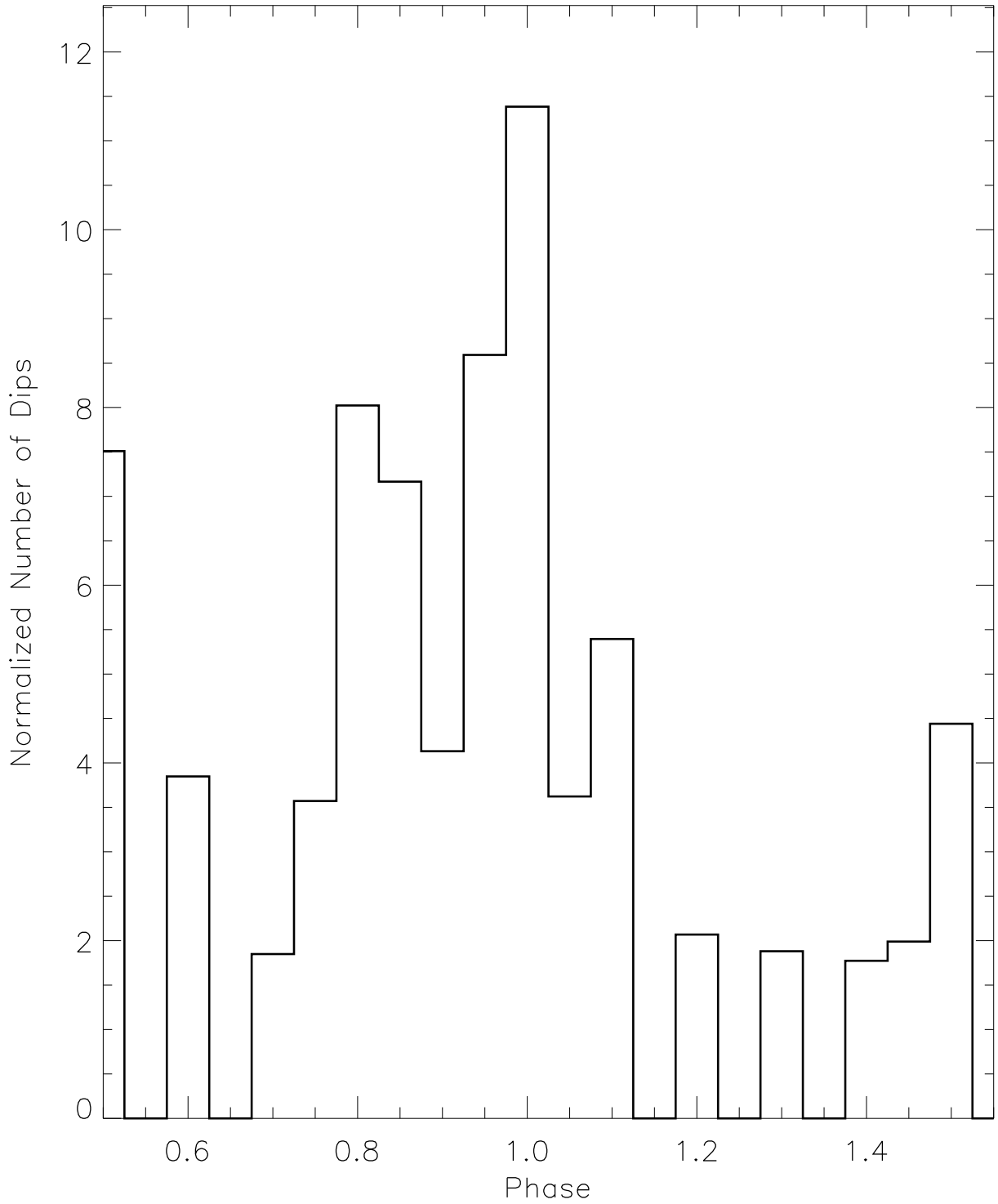


Fig. 2.— Orbital distribution of dips in Cyg X-1. The normalized number of dips in a phase bin is derived by dividing the actual number of dips seen in the phase bin by the fractional coverage of the bin (i.e., it represents the number of dips that would have been detected had the phase bin been fully covered by the observation).

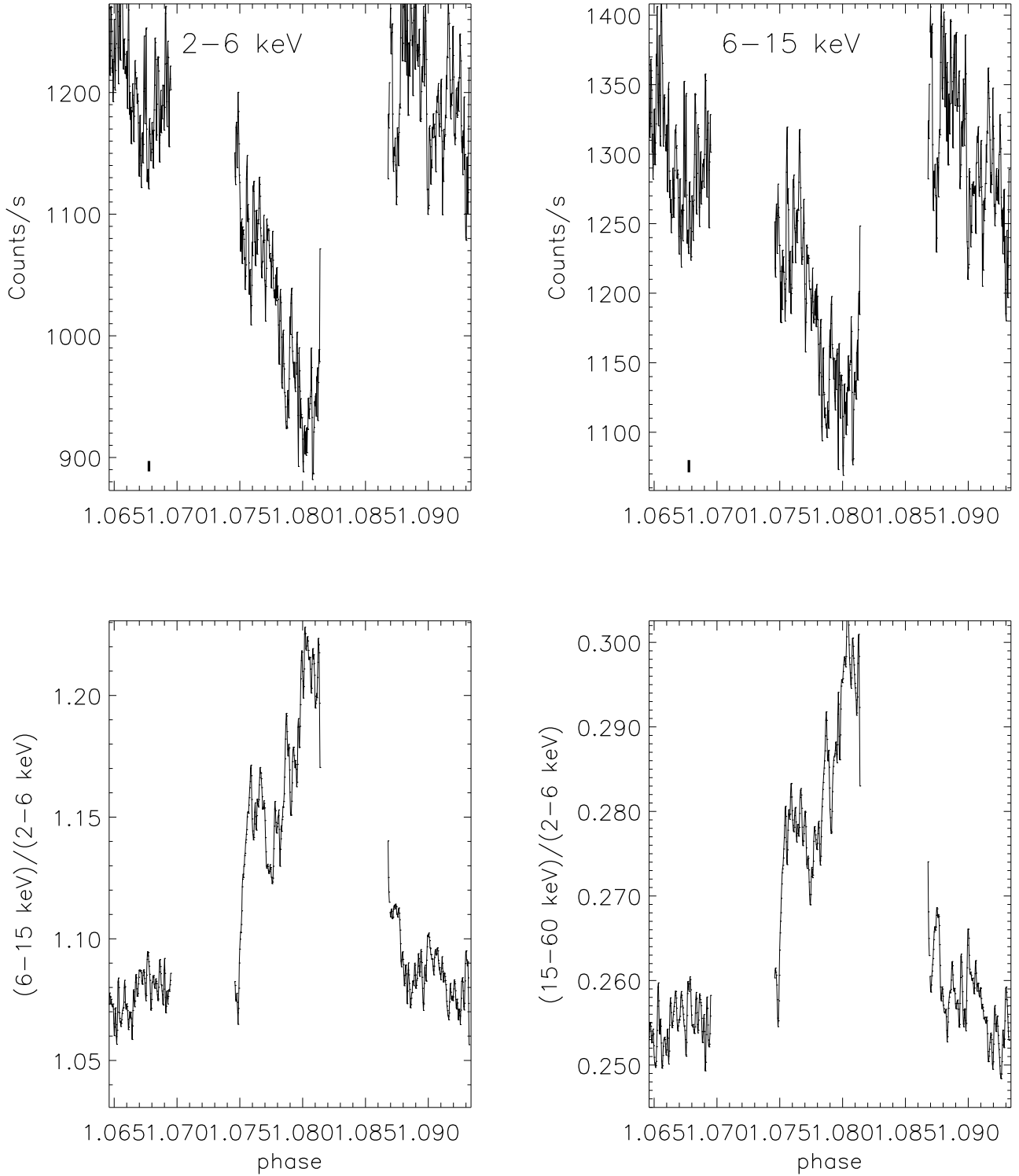


Fig. 3.— Same as Figure 1, but for the longest dip detected (by visual inspection; see text). Note that it occurred almost exactly at the time of superior conjunction of the black hole and lasted for more than an hour.

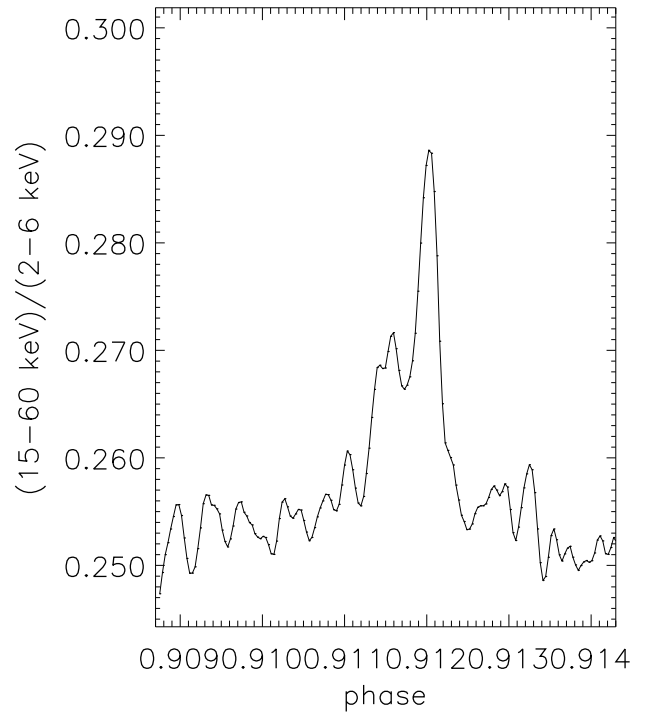
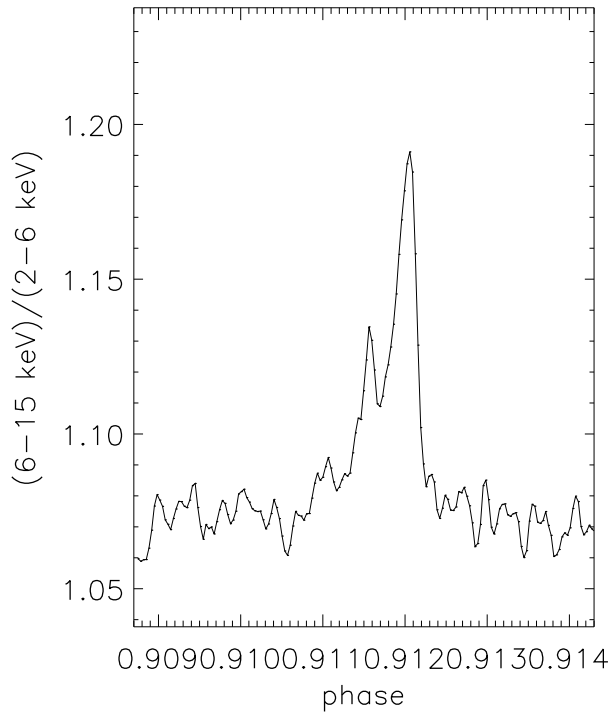
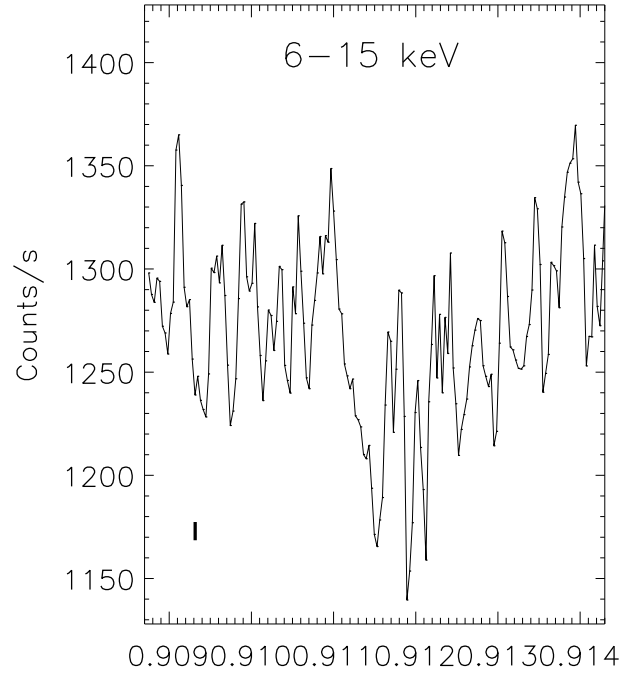
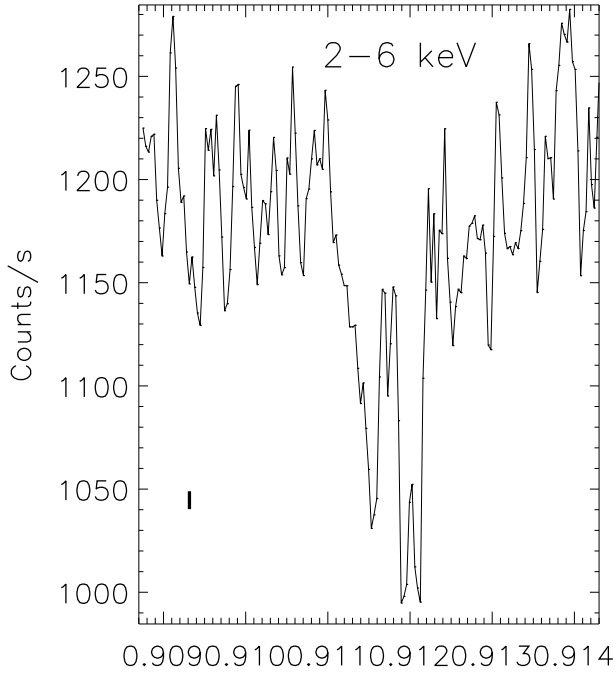


Fig. 4.— An example of an asymmetric dip profile.

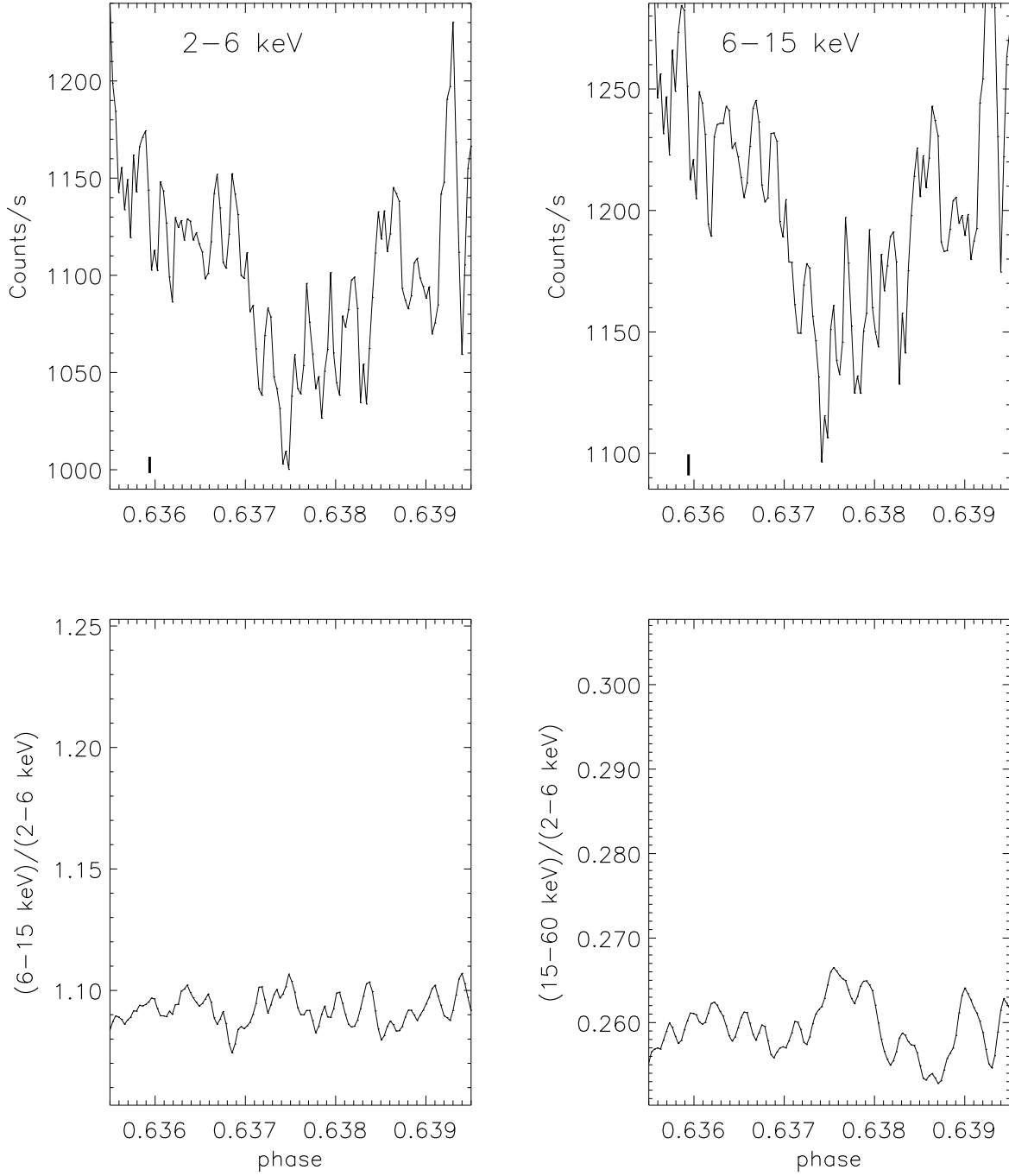


Fig. 5.— Same as Figure 1, but for a type B dip observed. For comparison, the vertical scales are adjusted to match those in Figure 1.

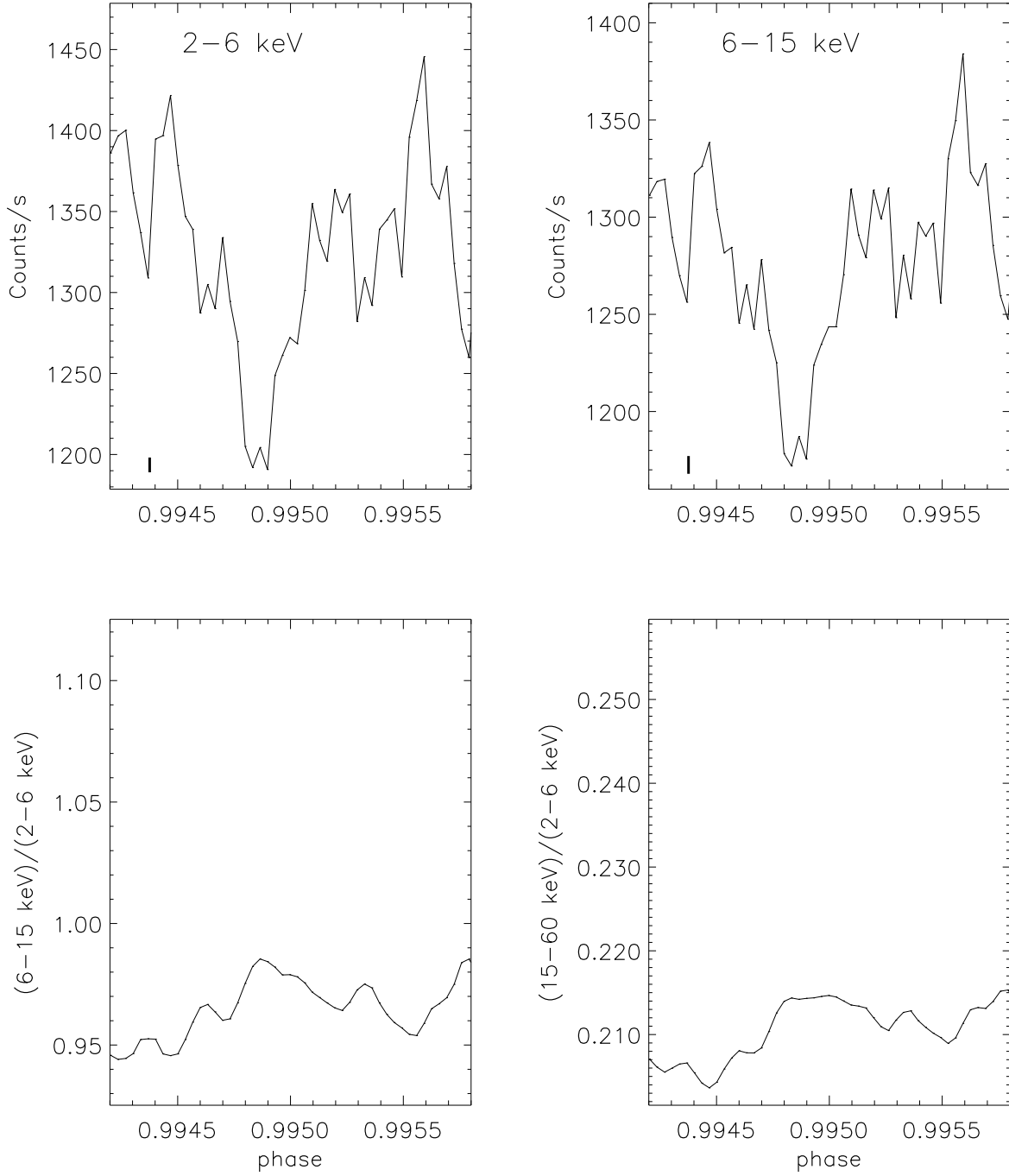


Fig. 6.— Same as Figure 1, but for a type B dip observed. For comparison, the vertical scales are adjusted to match those in Figure 1.

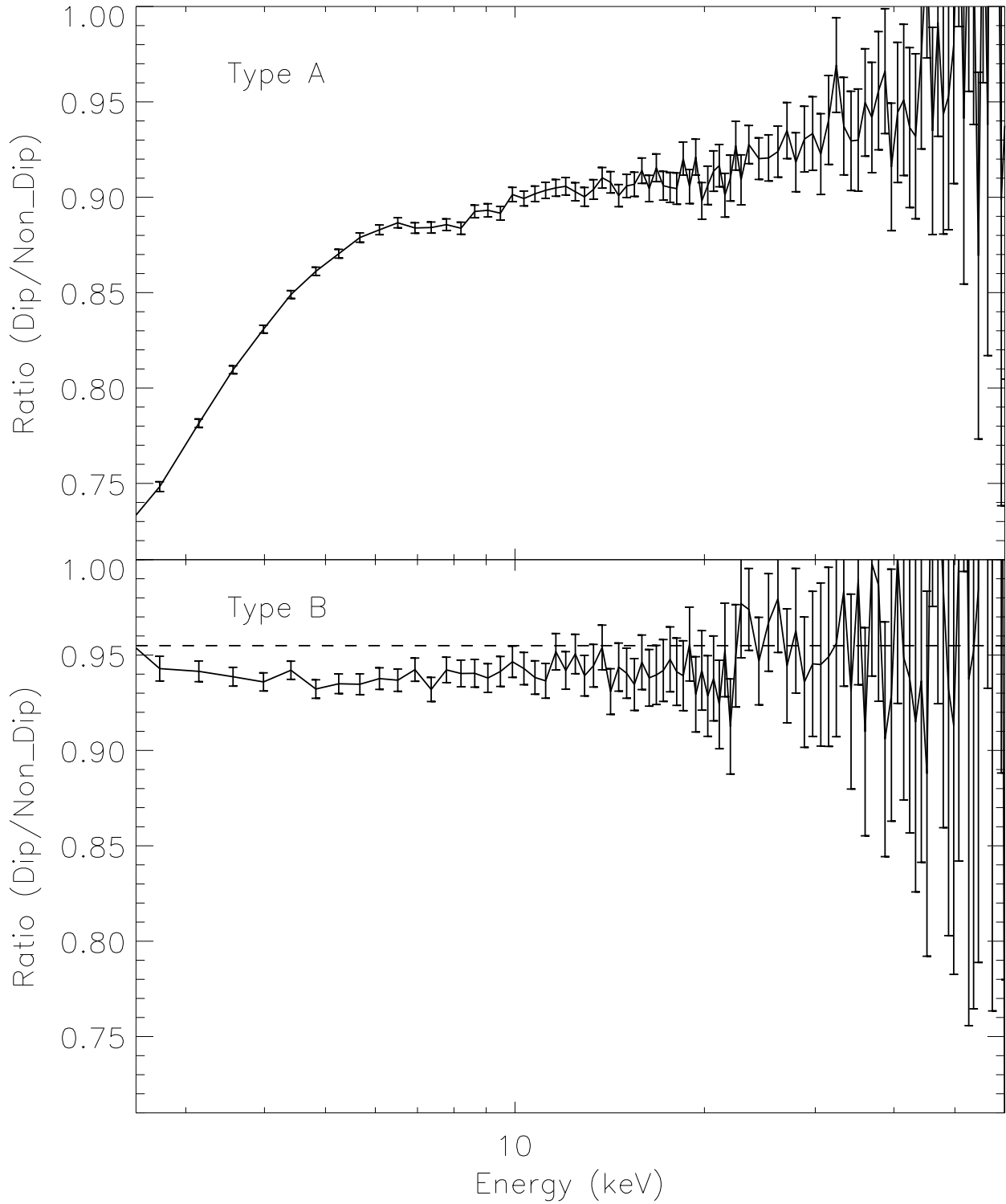


Fig. 7.— The ratio of dip spectrum to average non-dip spectrum for a type A dip (upper panel) and a type B dip (lower panel), respectively. The horizontal dashed line in the lower panel represents the average value of all points above about 20 keV.

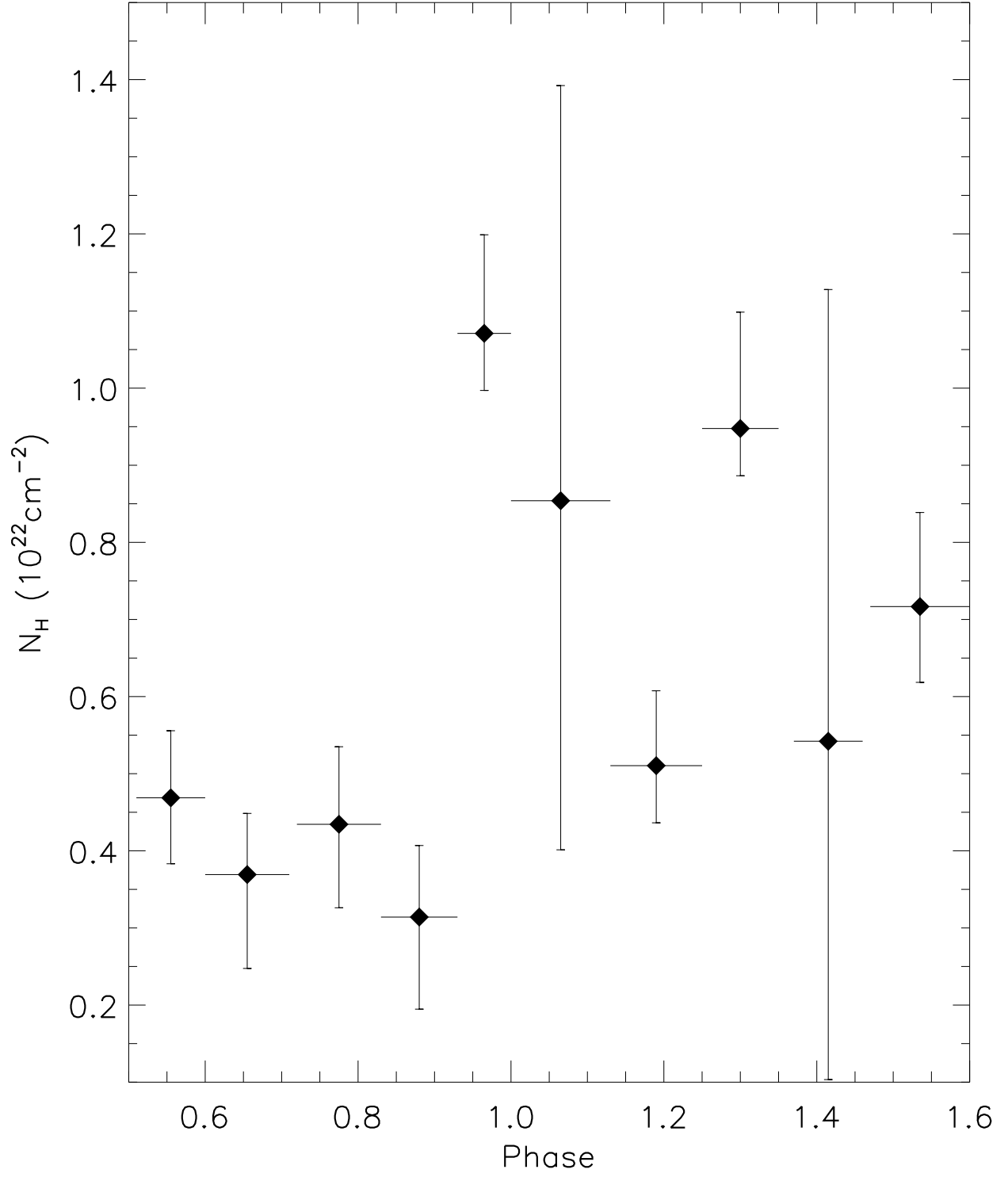


Fig. 8.— Observed variation in column density over one orbital cycle.